^{7}Li$(p, n)^7$Be cross section from threshold to 1960 keV and precise measurement of the ^{197}Au(n, γ) spectrum-averaged cross section at 30 keV

Guido Martín-Hernández,[1] Pierfrancesco Mastinu,[2] Elizabeth Musacchio González,[1,2]
Roberto Capote,[3] Hector Lubián,[1] and Miguel Macías[4]

[1]*Centro de Aplicaciones Tecnológicas y Desarrollo Nuclear, 30 No. 502 Miramar, La Habana, Cuba*
[2]*INFN - Laboratori Nazionali di Legnaro, Viale dell'Universita 2, 35020 Legnaro, Italy*
[3]*NAPC-Nuclear Data Section, International Atomic Energy Agency, A-1400 Vienna, Austria*
[4]*Universidad de Sevilla, Sevilla, Spain*

Background: The ^{7}Li$(p, n)^7$Be reaction is one of the most used nuclear reaction for accelerator-based neutron sources. There are few experimental cross section data in the double-value energy region and they are discrepant, as are the reaction yields.

Purpose: We derive the ^{7}Li$(p, n)^7$Be reaction cross section, and measure with small uncertainty the ^{197}Au$(n, \gamma)^{198}$Au spectrum-averaged cross section at neutron energy around 30 keV.

Method: By irradiating Li metal targets over the proton energy range of 1879 to 1960 keV, thick target yields were measured using the generated ^{7}Be activity. Based on the theoretical description of the reaction yield, accelerator parameters and reaction cross sections are derived. Gold foils were activated with the neutron field generated by the (p, n) reaction on a Li target at a proton energy of about a half keV above the reaction threshold.

Results: The thick target yield is well reproduced when the Breit-Wigner single-resonance formula for s-wave particles is used to describe the reaction cross section. The ratio between neutron and proton widths was found to be equal to $\Gamma_n/\Gamma_p = 5.4\sqrt{1 - T_{th}/T_p}$. The detailed balance principle is used to obtain the cosmologically important time-reversed ^{7}Be$(n, p)^7$Li reaction cross section. The measured ^{197}Au$(n, \gamma)^{198}$Au spectrum-averaged cross section agrees with the value calculated from the ENDF/B-VIII.0 library.

Conclusions: We demonstrated the feasibility of deriving the ^{7}Li$(p, n)^7$Be reaction cross section from the thick target yield. Using the ratio between neutron and proton widths obtained in this work reduces the uncertainty in calculating the reaction cross section to a factor of 2.3.

I. INTRODUCTION

The ^{7}Li$(p, n)^7$Be reaction is one of the most used nuclear reaction for accelerator-based neutron sources. Low threshold energy and high neutron yield make this reaction favorable for such a purpose. In addition, the neutron spectrum is satisfactory for applications such as cross section measurements for nuclear astrophysics [1,2] and boron neutron capture therapy [3,4].

In spite of the wide use of this reaction, the measured yield is discrepant from group to group and also among analytical calculations [5]. Furthermore, the reported reaction cross sections from different experiments are also discrepant from threshold up to 40 keV above it [6]. Both applications mentioned above use this proton energy range.

We have previously measured the shape of the reaction cross section from threshold up to 10 keV above it [7]. The aim of this work is to deduce the ^{7}Li$(p, n)^7$Be reaction cross section from the measured thick target yield in the proton energy range from threshold up to 80 keV above it.

Two additional subjects motivate this research. The first is related to the cosmological lithium problem. The ^{7}Be$(n, p)^7$Li reaction is responsible for most of the ^{7}Be destruction in the early Universe. The ^{7}Li primordial abundance depends on the ^{7}Be surviving fraction since ^{7}Be decays to ^{7}Li by electron capture. There is a strong disagreement between the prediction from the big bang nucleosynthesis theory and the observed primordial abundance of Li inferred from the observation of metal-poor stars [8]. The knowledge of the ^{7}Be$(n, p)^7$Li reaction cross section is crucial to determine the primordial abundance of Li in the Universe in model-based calculations. Therefore, a measurement of the ^{7}Li$(p, n)^7$Be reaction cross section and the application of the detailed balance principle to obtain the time-reversed ^{7}Be$(n, p)^7$Li reaction cross section will improve predictions of the primordial ^{7}Li abundance.

The second motivating issue is that, despite the fact that the ^{197}Au$(n, \gamma)^{198}$Au reaction has been extensively used as neutron monitor in the unresolved resonance region up to about 100 keV, it is only recognized as a standard at 0.0253 eV and between 0.2 and 2.5 MeV [9]. Benefiting from the deduced ^{7}Li$(p, n)^7$Be reaction cross section and based on the reaction kinematics, a small uncertainty measurement of the ^{197}Au$(n, \gamma)^{198}$Au spectrum-averaged cross section at neutron energy around 30 keV is performed.

II. ^{7}Li$(p, n)^7$Be REACTION YIELD

When irradiating a thick lithium target in its natural composition and in metal form with a proton beam of kinetic energy $T_p = T_{\text{beam}}$ larger than the reaction threshold T_{th}, the

thick target yield from the (p, n) reaction as a function of the reaction cross section $\sigma_{p,n}$ and the proton-on-lithium stopping power dT_p/dx reads as

$$Y_{p,n} = \frac{\chi\,\rho\,N_A}{e\,A_r} \int_{T_{th}}^{T_{\text{beam}}} \sigma_{p,n} \left(\frac{dT_p}{dx}\right)^{-1} dT_p, \tag{1}$$

where χ is the amount fraction of ^{7}Li in natural lithium (isotopic reference material), ρ is the Li density, N_A is Avogadro's number, e is the electronic charge, and A_r is the Li atomic weight. Both, the reaction cross section and the proton stopping power are a function of the proton energy.

In addition to $Y_{p,n}$, also of interest is the information on the ejected particle, the neutron. Therefore, the integral in Eq. (1) is conveniently expressed in terms of neutron emission angle and energy.

Naturally, the connection between the energy and angle of the outgoing particle and the energy of the incoming one is established by the two-body reaction kinematics. A detailed description of the reaction kinematics and yield can be found in Ref. [10] and in the works of Ritchie [11] and Lee and Zhou [12]. Here, we summarize the equations used in this work. All magnitudes are related to the laboratory system of reference.

Using the masses of the nuclei involved in the reaction, $M_{\text{Li}}, M_p, M_n, M_{\text{Be}}$, the incident proton energy T_p, and the neutron emission angle θ, the set of parameters Q, T_{th}, T_b (the energy limit above which the neutrons are emitted with a single energy), t_1, t_2, and t_3, defined as

$$Q = M_p + M_{\text{Li}} - (M_n + M_{\text{Be}}) = -1644.28 \text{ keV}, \tag{2}$$

$$T_{th} = -Q\left(1 + \frac{M_p}{M_{\text{Li}}} - \frac{Q}{2M_{\text{Li}}}\right) = 1880.61 \text{ keV}, \tag{3}$$

$$T_b = -Q\left[1 + \frac{M_p}{M_{\text{Li}} - M_n} - \frac{Q}{2(M_{\text{Li}} - M_n)}\right]$$
$$= 1920.30 \text{ keV}, \tag{4}$$

$$t_1 = 2M_p M_n T_p \left\{ 2\left(1 + \frac{T_p}{2M_p}\right)\cos^2\theta \right.$$
$$+ \frac{M_{\text{Be}}(M_{\text{Li}} + M_p)Q\left(1 + \frac{Q}{2M_{\text{Be}}}\right)}{M_p M_n T_p}$$
$$+ \frac{M_p^2 - M_{\text{Li}}^2 + M_n^2}{2M_p M_n} + \frac{4(M_{\text{Li}} - M_n)(M_{\text{Li}} + M_p)}{2M_p M_n}$$
$$\left. \times \left[1 + \frac{T_p}{2(M_p + M_{\text{Li}})}\right]\right\}, \tag{5}$$

$$t_2 = 2M_p T_p \left(1 + \frac{T_p}{2M_p}\right)\cos^2\theta \left\{ 4M_{\text{Li}}^2 (T_p^2 - T_{th}^2) \right.$$
$$+ 4M_{\text{Li}}(T_p - T_{th})[(M_p + M_{\text{Li}})^2 - (M_n^2 + M_{\text{Be}}^2)]$$
$$\left. - 8M_p M_n^2 T_p \left(1 + \frac{T_p}{2M_p}\right)\sin^2\theta \right\}, \tag{6}$$

and

$$t_3 = 2(M_{\text{Li}} + M_p)^2 \left\{ 1 + \frac{2T_p\left[1 + \frac{T_p}{2(M_{\text{Li}} + M_p)}\right]}{M_{\text{Li}} + M_p} \right.$$
$$\left. - \frac{2M_p T_p\left(1 + \frac{T_p}{2M_p}\right)\cos^2\theta}{(M_{\text{Li}} + M_p)^2} \right\}, \tag{7}$$

are calculated to assist in computing the neutron energy

$$T_n = \frac{t_1 \pm \sqrt{t_2}}{t_3}. \tag{8}$$

On the other hand to calculate $Y_{p,n}$ some functional forms for the reaction cross section and the proton-on-lithium stopping power are used. As suggested by Newson *et al.* [13] the reaction cross section from the threshold to approximately 1950 keV can be described by a Breit-Wigner single-resonance shape. The formula is reduced to

$$\sigma_{p,n} = \frac{4\pi\,g(J)}{k_p^2} \frac{\frac{\Gamma_n}{\Gamma_p}}{\left(1 + \frac{\Gamma_n}{\Gamma_p}\right)^2}, \tag{9}$$

where $g(J) = \frac{5}{8}$ is the statistical factor for the total angular momentum and $k_p = \frac{p}{\hbar}$ is the proton wave number and can be approximated to $k_p^2 = 3.6871 \times 10^{-3} T_p$. In this work the proton kinetic energy is always used in units of keV.

The ratio between neutron and proton widths is calculated as $\Gamma_n/\Gamma_p = C_\circ\sqrt{1 - T_{th}/T_p}$, and $C_\circ$ is a parameter determined from the experiment. After transforming Eq. (9), $\sigma_{p,n}$ in unit of barns is calculated as

$$\sigma_{p,n} = \frac{2130\,C_\circ\sqrt{1 - \frac{T_{th}}{T_p}}}{T_p\left(1 + C_\circ\sqrt{1 - \frac{T_{th}}{T_p}}\right)^2}. \tag{10}$$

Proton stopping power in unit of keV/cm, based on calculation using SRIM [14], is parametrized as

$$\frac{dT_p}{dx} = \frac{2.7463 \times 10^7}{T_p^{0.77866}}. \tag{11}$$

With the use of two additional kinematic parameters γ and ξ, defined as

$$\gamma = \sqrt{\frac{M_p M_n M_p}{M_{\text{Be}}(M_{\text{Li}} - Q)(T_p - T_{th})}} \tag{12}$$

and

$$\xi = \sqrt{\gamma^{-2} - \sin^2\theta}, \tag{13}$$

the double-differential yield $Y(T_p, \theta)$ is written in the following form:

$$Y(T_p, \theta) = \pm \frac{\chi\,\rho\,N_A}{e\,A_r} \frac{\sigma_{p,n}}{4\pi}\left(\frac{dT_p}{dx}\right)^{-1}$$
$$\times \frac{\gamma(\cos\theta \pm \xi)(M_{\text{Be}} + M_n)^2}{M_p M_n \xi(\cos\theta \pm \xi) \pm M_{\text{Be}}(M_{\text{Li}} - Q)\frac{T_{th}}{T_p}}. \tag{14}$$

TABLE I. Values of constants used in this work.

Quantity	Symbol	Value	Unit	Source
Atomic mass unit	u	931494.0954	keV	[17]
Proton mass	M_p	1.007276466583	u	[15]
Neutron mass	M_n	1.008664915823	u	[16]
^{7}Li mass	M_{Li}	7.014357754615	u	[16], adjusted using M_p
^{7}Be mass	M_{Be}	7.014734515676	u	[16], adjusted using M_p
^{7}Li atomic fraction	χ	0.9241		[18]
Li atomic weight	A_r	6.94		[18]
Li density	ρ	0.534	g cm^{-3}	[19]
Avogadro's number	N_A	$6.022140857 \times 10^{23}$	mol^{-1}	[20]
Elementary charge	e	$1.6021766208 \times 10^{-19}$	C	[20]
Planck's constant over 2π	$\hbar$	$6.582119514 \times 10^{-19}$	keV s	[20]
Speed of light in vacuum	c	299792458	m s^{-1}	[20]

A computer code named PLINBE has been developed. In this code, a scan of a (T_p, θ) grid with a 0.18° step for θ, ranging from 0° to 180°, and a 10^{-4} keV step for T_p, ranging from T_{th} to $T_{max} = 1960$ keV, is performed. In the proton energy range from T_{th} to T_b the neutron energy is double valued, which is noticeable in the $\pm$ sign in previous equations, and neutrons are emitted in the forward hemisphere. For each angle lower than 90°, T_p is varied from T_b down to T_s using the negative sign and from T_s up to T_{max} using the positive sign in both Eqs. (8) and (14) to obtain $T_n(T_p)$ and $Y(T_p)$. T_s is the proton energy that satisfies $t_2 < 0$. For angles equal to or larger than 90°, where the neutron energy is unique for a given T_p and θ, T_p is varied from T_b up to T_{max} using the negative sign in Eq. (8) and the positive one in Eq. (14).

Thereafter $T_n(T_p)$ and $Y(T_p)$ are transformed into $T_p(T_n)$ and $Y(T_n)$ by cubic spline interpolation with a neutron energy step of 0.1 keV. When all angles are evaluated, two matrices are generated, $T_p(T_n, \theta)$ and $Y(T_n, \theta)$. The latter is the double-differential neutron yield $d^2y(T_n, \theta)/d\Omega dT_n$. By integrating it over the solid angle and energy, Eq. (1) is rewritten as

$$Y_{p,n} = 2\pi \int_{T_n^{min}}^{T_n^{max}} \int_0^{\theta^{max}} \frac{d^2y(T_n, \theta)}{d\Omega \, dT_n} \sin\theta \, d\theta \, dT_n, \quad (15)$$

where T_n^{min} and T_n^{max} are the neutron minimum and maximum energies, and θ^{max} the maximum neutron emission angle. The three magnitudes are a function of T_{beam}.

The values of the constants used in this work are listed in Table I. A new value for M_p [15] was reported after the current atomic mass evaluation [16], therefore the ^{7}Li and ^{7}Be masses are adjusted using this value.

In practice, the effective projectile energy producing the nuclear reaction is a distribution rather than a single value. This is due to the combined influence of beam energy spread and thermal motion of target atoms. These effects modify the shape of the thick target yield behavior at proton energies near T_{th}. In order to account for these effects, the proton energy is considered to be a Gaussian distribution. This distribution is folded into Eq. (15). Figure 1(a) shows the calculated $Y_{p,n}$ curves with our program PLINBE for several FWHM values. Figure 1(b) shows the second derivatives of $Y_{p,n}$ curves where their maximum values are slightly shifted to the right of T_{th};

nevertheless they are usable for accelerator energy calibration purposes.

III. EXPERIMENT

The experiment was carried out at the 7-MV CN Van de Graaff accelerator in the Laboratori Nazionali di Legnaro. In CW mode a proton beam of some μA is transported to the target. The proton energy is established by setting the current, hence the magnetic field B, of a 90° analyzing magnet and at the same time, via a feedback circuit, setting the corresponding voltage (proton energy) in the accelerator column. A scan of the ^{7}Li(p, n)^{7}Be reaction from T_{th} up to T_{max} is performed. For each proton energy, a freshly prepared lithium target is irradiated. During the irradiation period the current
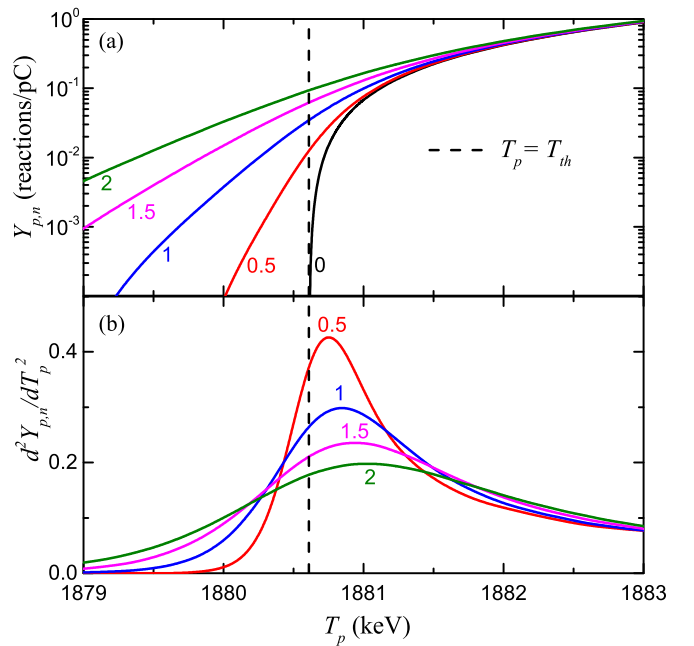

FIG. 1. (a) Calculated thick target yield curves for different proton energy spreads (FWHM = 0, 0.5, 1, 1.5, and 2 keV) and (b) their second derivatives.
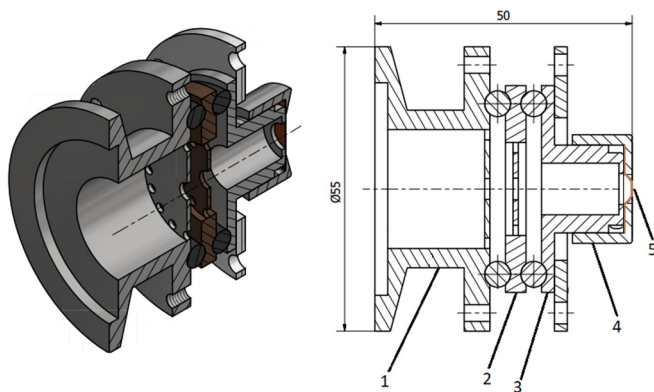
FIG. 2. Target assembly drawing. Main parts: **1**-collimator, **2**-electron rejection electrode, **3**-target holder, **4**-nut, and **5**-target backing. Dimensions are in millimeters, and all parts are to scale except for the target backing thickness.

is measured and recorded every second. The accelerator was never switched off during the whole experiment and the optics of the beamline after the analyzing magnet unchanged.

The target assembly, represented in Fig. 2, is formed by a collimator **1** with a 4 mm diameter aperture, an electron rejection electrode **2** with a 4.2 mm diameter aperture, and a target holder **3** with an 8 mm diameter aperture and its nut **4**. A removable 0.1 mm-thick copper foil **5**, onto which the lithium is deposited, closes the target assembly.

The nut presses the copper backing against the target holder achieving a vacuum-tight union. At the target position, a vacuum level of the order of 10^{-5} mbar was reached. Parts **1**, **2**, and **3** are electrically isolated. Parts **4** and **5** are in contact with part **3**. The collimator is connected to ground and the electron rejection electrode is biased to -300 V respect to the target. The latter is connected to ground through a 100 kΩ resistor. The measured voltage drop on this resistor is used to calculate the beam current. By applying an air flow to the external face of the copper backing, heat removal is achieved.

The beam travels inside the target assembly from left to right. The target backing is slightly curved approaching the end plane of the target assembly. This was done in order to have to gold foil as close as possible to the neutron producing surface. The gold foil is used in the ^{197}Au neutron activation experiment explained at the end of this section. The target active area defined by the collimator remains flat.

By visual inspection of the beam using a quartz window at the target position (without collimator), a horizontal oscillation of the beam of about 1 Hz, larger than the collimator diameter, was visible. This is probably produced by a small mechanical oscillation around the vertical axis of the accelerator column. This casual event produces a beam sweeping over the collimator hole leading to a homogeneous target illumination in a 4 mm diameter surface (surface source).

The lithium targets are produced inside an argon-filled glovebox from a natural lithium metal bar. The raw material which is stored in paraffin oil is dried, peeled off, cut in slices, rolled down to about 0.25 ± 0.05 mm thickness, cut into 8 mm diameter disks, and attached by pressing against the copper backing. A gate valve is coupled to the target

assembly next to the collimator, allowing operations with the target without exposing it to air. The targets are kept either under argon or in vacuum at all times. After the irradiation, the target assembly is taken back to the glovebox and the target is removed and stored.

Per each occurred (p, n) reaction a radioactive ^{7}Be nuclei is formed. Part of the generated radioactivity during the irradiation is measured with a 60.5 mm diameter and 52.5 mm height high-purity germanium (HPGe) detector or a 38 mm diameter and 38 mm height LaBr$_3$ detector. Two detectors were necessary due to the number of samples to be measured and the limited time availability of the HPGe detector. For the radioactivity measurements, the targets are remounted into the target assembly and placed in touch with the detector window in the case of the HPGe and with the housing in the case of the LaBr$_3$. During the radioactivity measurement the target is kept under argon to avoid oxidation and consequently thickness and material modification.

The thick target yield, expressed in reactions/C [21], is calculated from the area A under the photopeak corresponding to the 478 photons from the ^{7}Be decay as

$$Y_{p,n} = \frac{\lambda A}{I \, \epsilon_\gamma \, P_\gamma (1 - e^{-\lambda t_i}) e^{-\lambda t_w} (1 - e^{-\lambda t_m})}, \qquad (16)$$

where I is the average proton current on target during the irradiation time t_i, ϵ_γ is the detection efficiency, $P_\gamma = 0.1044$ is the photon emission probability per decay [22], $\lambda = \ln 2 \, (t_{1/2})^{-1}$ is the decay constant, $t_{1/2} = 53.22$ d is the half-life [22], and t_w is the elapsed time between irradiation and the beginning of the measuring time t_m. Due to the accelerator stable condition (constant current) during each irradiation and the ratio between irradiation time and ^{7}Be half-life, the correction due to current variation during irradiation is negligible. The same applies to the gold activation experiment.

The 478 keV photon detection efficiency for both detectors was measured using one of the irradiated lithium targets as a ^{7}Be calibration source. The activity of this source was measured with the HPGe detector. A set of point-like calibration sources composed of ^{22}Na, ^{54}Mn, ^{60}Co, ^{133}Ba, ^{137}Cs, and ^{152}Eu were used to determine the detection efficiency at 125 mm from the HPGe detector window. At this distance, dead time losses were reduced to a range from 4% to 15%, and the point-like condition for the ^{7}Be calibration source was achieved. Coincident summing effects was found to be negligible at this position. The correction due to geometrical differences between calibration sources and the ^{7}Be calibration source was calculated by Monte Carlo simulation and found to be negligible. All Monte Carlo simulations were performed using MCNP [23].

At proton energies below 1880.8 keV it was impractical to measure the target radioactivity due to the required long measurement times. Instead, the neutron emission N_n is measured. A 5 cm diameter and 2.5 cm thickness ^{6}Li-loaded glass detector covered by 0.6 cm of lead and 2 cm of high-density polyethylene is located at about 15 cm from the lithium target at zero degrees with respect to the proton beam direction. The polyethylene is added to increase the detection efficiency for 29.7 keV neutrons, the neutron energy at T_{th}. The lead layer located in front of the glass is used to reduce the

copious γ yield produced by the ^{7}Li$(p, p'\gamma)^7$Li and the γ rays produced by the neutron capture in hydrogen. The signal from the detector is fed to a multichannel analyzer and, after background subtraction, the area under the neutron peak is calculated and divided by the total charge on target during the irradiation.

In order to establish the relationship between magnetic field and proton energy, we have performed proton time-of-flight spectrometry. The beam is switched to pulsed mode. With a frequency of 3 MHz, 2 ns width proton bunches are produced. Two beam pickup capacitors are inserted in the horizontal beamline: one immediately after the analyzing magnet and the other located about 10 m from the first, just before the target. The signals induced when the proton beam of variable current (pulsed) passes through the pickups are digitized and analyzed. The time difference between the two signals, corrected for the signal delay times of the cables and electronics is measured.

Using its mass at rest $u M_p$ and the speed of light c, the proton kinetic energy is calculated as

$$T_p = u M_p \left[\frac{1}{\sqrt{1 - \left(\frac{x}{ct}\right)^2}} - 1 \right], \qquad (17)$$

where t is the time used by the proton to travel the distance x. This measurement is taken for different magnetic fields, and an empiric relationship between B and T_p is established.

In Eq. (17) only the distance x (proton flight path) remains to be measured. The presence of active elements in the beamline such as focusing magnets and lenses modify the beam trajectory, hence the linear distance measured between the pickups does not necessarily agree with the distance traveled by the beam. To determine the real distance traveled by the beam a scan of the reaction threshold is performed and the field at T_{th} is estimated by maximizing the second derivative $d^2 N_n / dB^2$ as proved in Sec. II. As a first-order approximation, the flight path is adjusted to have this point (B close to threshold) belonging to the curve that relates B and T_p.

The measurement of the ^{197}Au$(n, \gamma)^{198}$Au spectrum-averaged cross section is performed by irradiating gold foils and measuring the generated radioactivity. The irradiation was performed twice using a different foil per irradiation, each of about 0.1 mm thickness, 12 mm diameter, and 99.99% purity from Goodfellow. The foil is located centered and perpendicular to the proton beam direction in touch with the target external surface. The neutron path between its generation point and the gold foil is intersected by the target structure (0.25 mm of Li and 0.1 mm of Cu). The presence of these materials somehow modifies, due to scattering and capture, the total amount of neutrons reaching the Au foil. This is considered later as a correction due to target structure.

Gold activation was performed with the neutron field generated by protons with $T_p = 1881.08$ keV and a FWHM = 1.25 keV. Figure 3 plots (a) the calculated neutron energy spectrum dY/dT_n and (b) the angular distribution $dY/d\theta$, produced by the ^{7}Li$(p, n)^7$Be reaction for the selected proton energy. These distributions are calculated with PLINBE.

At the end of the irradiation, the activated foil was immediately transferred to the HPGe detector for the activity
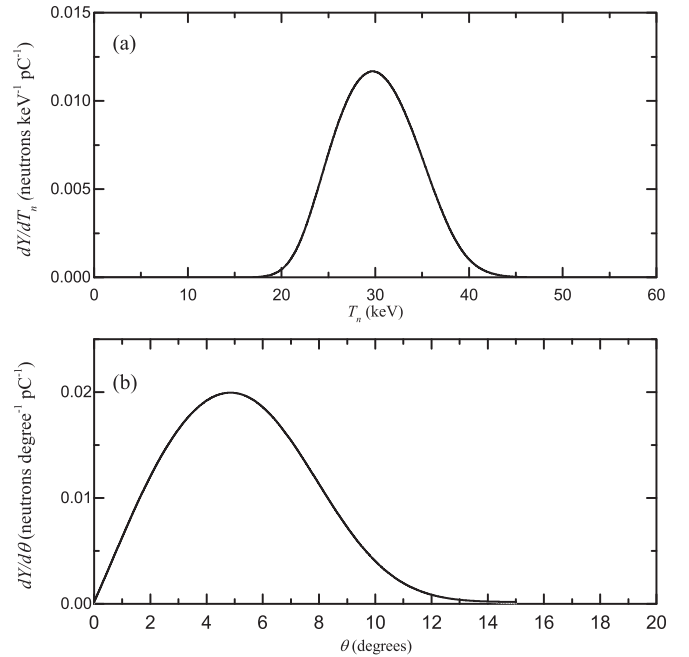

FIG. 3. (a) Calculated neutron energy spectrum and (b) angular distribution, produced by the ^{7}Li$(p, n)^7$Be reaction with a proton beam of $T_p = 1881.08$ keV and a FWHM = 1.25 keV.

measurement. The foil is placed, centered, on top of the detector window. The number of ^{198}Au nuclei formed per incident neutron during the irradiation is calculated from the area A under the photopeak, corresponding to the ^{198}Au decay as

$$Y_{n,\gamma} = \frac{\lambda A}{Y_{p,n} I \epsilon_\gamma P_\gamma (1 - e^{-\lambda t_i}) e^{-\lambda t_w} (1 - e^{-\lambda t_m})}, \qquad (18)$$

where $Y_{p,n}$ is obtained from Eq. (16). The remaining parameters have the same meaning as in Eq. (16) but corresponding to the ^{198}Au decay with $P_\gamma = 0.9562$ and $t_{1/2} = 2.6941$ d [24].

The spectrum-averaged cross section reads as

$$\langle \sigma_{n,\gamma} \rangle = F_x \frac{Y_{n,\gamma}}{n_s}, \qquad (19)$$

where the areal density n_s is the number of Au atoms per unit of area in the samples and F_x is a correction factor to account for experimental influences such as surface source, target structure (both explained above in this section), finite sample thickness, and flat sample. The last two experimental conditions produce the major contribution to F_x. The fact that the sample has a finite thickness produces multiple scattering while flat sample yields higher interaction probability for higher neutron emission angles. All of these facts are taken into account by Monte Carlo simulation of the experiment.

IV. RESULTS

A. Detection efficiency

Figure 4 plots the detection efficiency at the calibration position for the HPGe detector. The detection efficiency for 478 keV photons is equal to 0.0035 ± 0.0001 as obtained
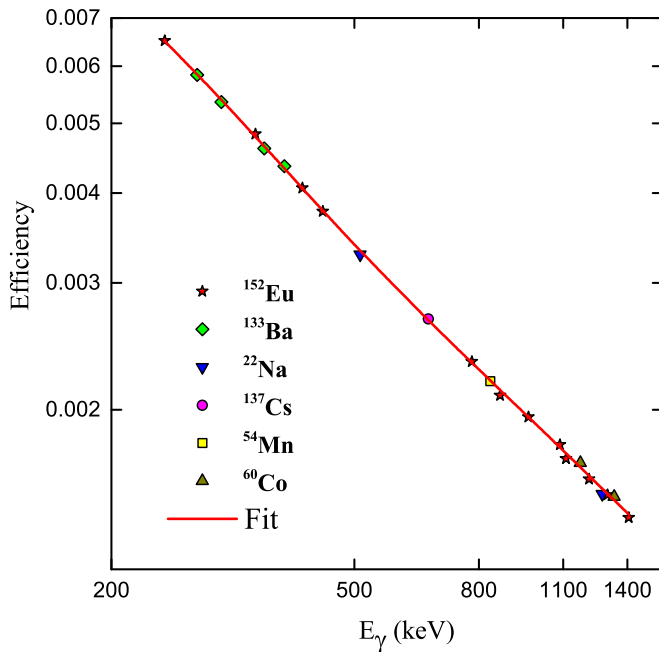
FIG. 4. HPGe detection efficiency measurement with the calibration sources located at 125 mm from the detector window.

FIG. 5. Scan of the reaction threshold. N_n is the number of detected neutrons per unit of charge.

by interpolating the fitted data. The data were fitted with a double exponential decay function. Then, the activity of the ^{7}Be reference source was measured. Afterward, the reference source was located at zero distance from the detector window (measuring position) to measure the efficiency, attaining a value of $\epsilon_{478} = 0.0875 \pm 0.0026$ for the HPGe detector and 0.0613 ± 0.0018 for the LaBr$_3$ one.

As a consequence of the uncertainty from the activity of the calibration sources, the uncertainty in the efficiency determination is 3%. The remaining uncertainties in the magnitudes involved in the efficiency or activity determination have a negligible impact on the overall uncertainty. Additionally, it was experimentally determined that variations in sample positioning have an unimportant influence on these radioactivity measurements.

The detection efficiency ϵ_γ for the 412 keV line is determined relative to the measured ^{7}Be line detection efficiency as $\epsilon_\gamma = \epsilon_{478} F_c (\frac{\epsilon_{412}}{\epsilon_{478}})_{125\,mm}$. The ratio $(\frac{\epsilon_{412}}{\epsilon_{478}})_{125\,mm}$ is calculated from the measured efficiencies at 125 mm, and F_c is a correction factor due to geometry differences between the reference source and the Au foil, including γ ray absorption in the Au foil. F_c was calculated by Monte Carlo simulation of the measuring setup.

B. Accelerator calibration

The result from the scan of the reaction threshold by counting the forward-directed neutron emission is reported in Fig. 5. When total neutron counting is used, the neutron intensity shows a sustained increase according to Eq. (1), where the reaction cross section and the proton stopping power are calculated using Eqs. (10) and (11). This is visible in Fig. 1(a).
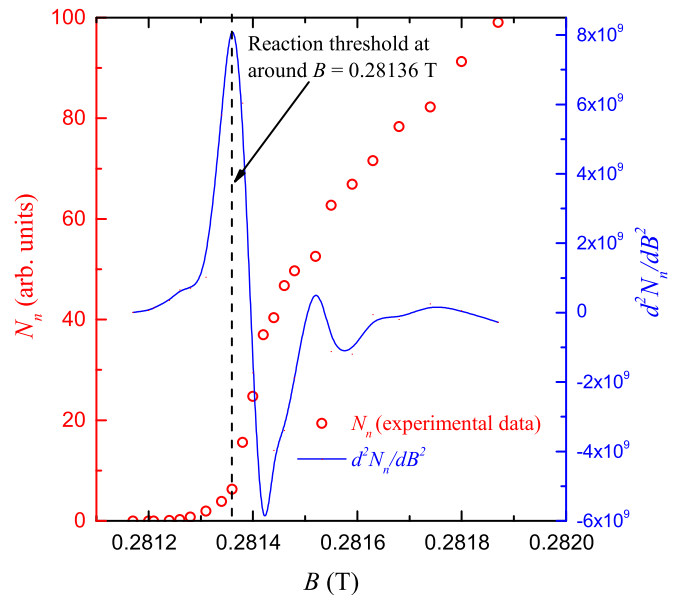
Such behavior is not apparent in Fig. 5. In contrast, at $B = 0.28140$ T the yield rate departs from the theoretical prediction. This is due to the fact that the neutron detector was distanced from the target to avoid pulse pileup. The detector covers a semi-angle of the neutron emission cone of about $9°$, producing a kinematic collimation where only neutrons originated from protons with $T_p < T_{th} + 1$ keV pass through the detector.

The approximated value for B at T_{th} is determined from the maximum of d^2N_n/dB^2 and is equal to 0.28136 T. This value is used next to establish the relation between magnetic field and proton energy. According to Fig. 1(b) the field at T_{th} is expected to be slightly lower, depending on the beam energy spread.

Proton energy spectra are measured for different magnetic fields as shown in Fig. 6(a). More than 5×10^5 protons are collected for each field. They are normalized to unit area. For the pulsed beam used in this determination, the FWHM of the proton distributions is around 1.7 keV. Figure 6(b) shows the quadratic relation between magnetic field and proton energy.

The quadratic relation reproduced in Fig. 6(b) is actually obtained after a fitting process of the reaction yield, that will be explained in Sec. IV C. According to this relation, the proton energy at $B = 0.28136$ T is about 0.4 keV above T_{th}. This offset is consistent with the theoretical prediction reproduced in Fig. 1(b).

C. Thick target yield

The measured thick target yield is reported in Fig. 7. There are three regions on this plot. The higher energy region corresponds to yield values calculated from the induced ^{7}Be activity in the target using Eq. (16). A lower energy region corresponds to the neutron activity which was scaled up. A third, intermediate region is formed by three energy points
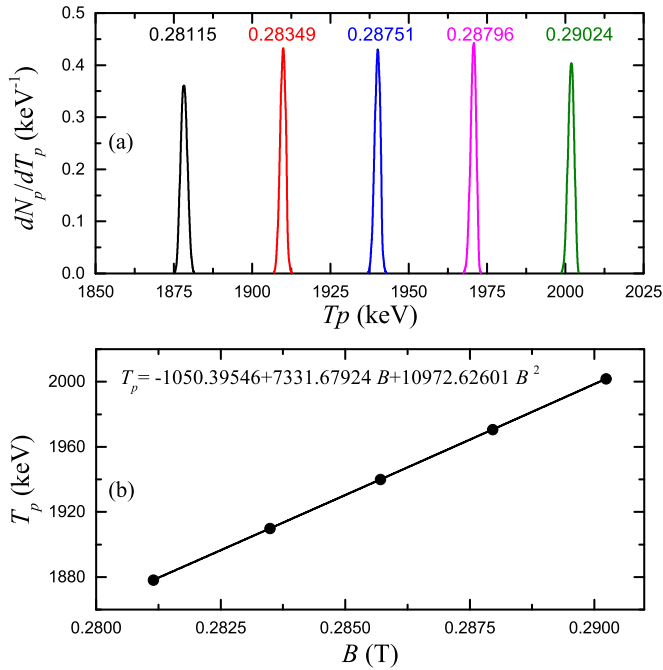
FIG. 6. (a) Proton distributions measured via time-of-flight for different magnetic field values. (b) Relationship between magnetic field and proton energy.

where both ^{7}Be and neutron activities are measured in order to scale up the neutron activity to that of ^{7}Be. In this way, the neutron detection efficiency is accounted for. The requirement to perform this operation is that the neutron detection efficiency does not change significantly within this proton
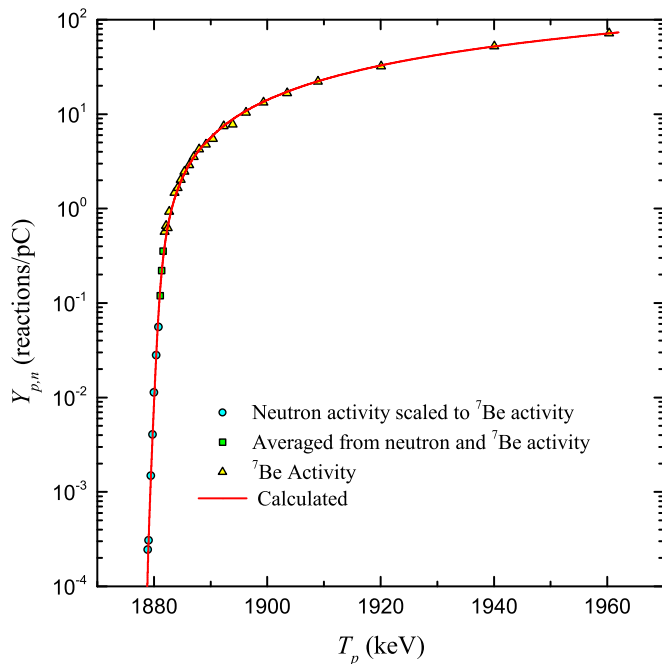

FIG. 7. Measured and calculated thick target yield for the ^{7}Li(p, n)^{7}Be reaction.

energy range. It was experimentally verified that when the proton energy approaches from high energies to the reaction threshold, the ratio between both activities tends to a constant value. This was also confirmed by Monte Carlo simulation. Although the yield changes very rapidly at proton energies just above the threshold, the emitted neutron spectrum does not.

The statistical uncertainty on the activity determination was kept below 0.2% and charge measurement has a 0.1% uncertainty. Experimental thick target yield shows a 3% uncertainty mainly due to the efficiency determination. The remaining uncertainties in the magnitudes involved in thick target yield determination have a negligible impact on the overall uncertainty.

$Y_{p,n}$ data are originally taken as a function of the magnetic field in the analyzer. The conversion from field to energy values is made in conjunction with the determination of the theoretical yield. This is based on a fitting procedure of the experimental values using the program PLINBE, the empirical relationship between magnetic field and proton energy, and the well-known reaction threshold energy. The goal of this fitting is to determine the theoretical $Y_{p,n}$ curve that best reproduces the experimental data and at the same time establishes the connection between proton energy and magnetic field. The result of this fitting is shown Fig. 7, labeled "Calculated."

Three parameters were involved in the fitting process: two linked to the experimental conditions and one related to the nuclear reaction itself. The latter is discussed in Sec. IV D.

The two parameters related to the experimental conditions are the connection between magnetic field and proton beam energy, and the proton energy spread. The latter, expressed in terms of FWHM, influences only the shape of the low energy part [see Fig. 1(a)]. FWHM is known for the pulsed beam but unknown for the CW beam. The FWHM was found to be equal to 1.25 keV, a value that is predictably lower than the 1.7 keV of the pulsed beam. The bunching system used to reduce the time spread of the proton pulse increases the beam energy spread.

The accelerator energy calibration based on maximizing d^2N_n/dB^2 is expected to be near but not at the real value due to the effect of the beam energy spread and the precision of the reaction threshold scanning. Therefore, a second parameter related to the experimental condition is included: the proton flight path [x in Eq. (17)]. This value was found to be equal to 9.7973 ± 0.0001 m.

D. ^{7}Li(p, n)^{7}Be reaction cross section

The third parameter used in the fitting process to determine the theoretical thick target yield is $C_\circ$, used in Eq. (10) to calculate the reaction cross section. From the fitting process of our data, we found the numerical value of $C_\circ = 5.4 \pm 0.4$. The uncertainty in $C_\circ$ is derived from the uncertainties in $Y_{p,n}$ and in the absolute value of proton-on-lithium stopping power. Considering the 3% uncertainty in $Y_{p,n}$ determination, proton stopping power cannot sustain a variation (uncertainty) larger than 4%, otherwise $Y_{p,n}$ varies more than 3% for any given $C_\circ$. This result is consistent with the uncertainty estimation reported in Ref. [25,26] when SRIM is used to calculate
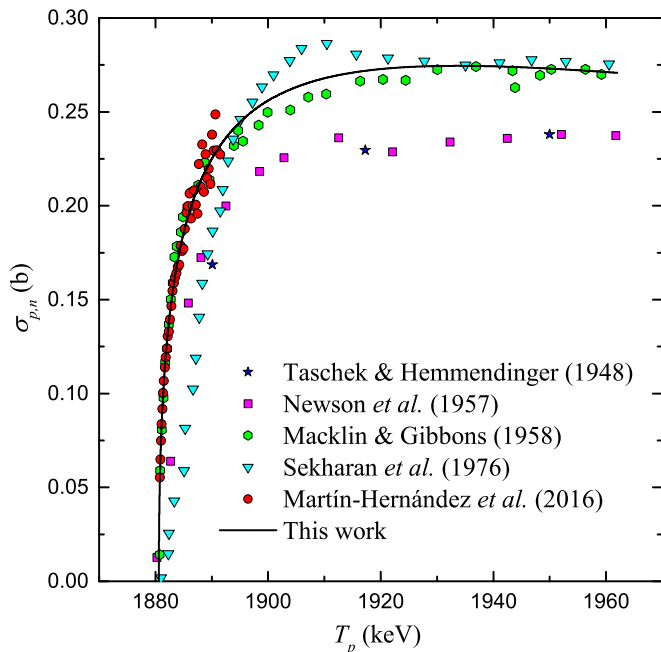
FIG. 8. The ^{7}Li$(p, n)^7$Be reaction cross section determined in this work compared with previous measurements.

charged particle stopping power. In previous works where $C_\circ$ was determined, the uncertainty was equal to or larger than 17% [13,27].

Figure 8 shows a comparison from all available cross section data. It contains four absolute cross section data [13,27–29], one cross section shape data [7], and the cross section derived in this work. The cross section data from Ref. [7] were normalized to the current work.

The data from Newson *et al.*, originally normalized to the absolute values of Taschek and Hemmendinger are in disagreement regarding its absolute value, but, if scaled up, they agree with our determination. There is a good agreement between our determination, Macklin and Gibbons's, and that of Sekharan *et al.*, above $T_p \approx T_b$. Below this value, the latter data are in visible disagreement with the remaining ones. As indicated by the authors this is due to some dependence (not accounted for) of the detection efficiency on the neutron emission angle. Our result concurs with the Macklin and Gibbons data and with renormalized Martín-Hernández *et al.* data along the measured energy range.

The single-level Breit-Wigner analysis is sufficient to account for all the neutron yield from T_{th} up to T_{max} due to the $J^\pi = 2^-$ state in the ^{8}Be nuclei. A multilevel-multichannel *R*-matrix analysis extended to a higher proton energy range will obviously include more states. This analysis will likely agree with the current results within the quoted uncertainties.

E. ^{197}Au$(n, \gamma)^{198}$Au spectrum-averaged cross section

The gold foils were irradiated with the neutron beam produced by the ^{7}Li$(p, n)^7$Be reaction using a proton beam selected by the analyzer with $B = 0.28136$ T. This field corresponds to a proton energy $T_p = 1881.08 \pm 0.06$ keV.

Table II lists the main parameters and the results from the activation of the two flat gold samples. Column 5 registers the total number of neutrons generated during the irradiation that produces the total number of ^{198}Au nuclei listed in column 6. The experimental reaction yield $Y_{n,\gamma}$ is calculated from Eq. (18), where relative detection efficiencies at 412 and 478 keV are needed. The uncertainty in the reaction yield is due to a 0.6% to 0.8% uncertainty from the counting statistic and 0.6% uncertainty from the determination of the efficiency ratio between the 478 and the 412 keV γ lines from ^{7}Be and ^{198}Au decays. The latter is calculated from the mean relative difference between the measured efficiency values and the function that fits those values.

The correction factor F_x is calculated from

$$F_x \frac{Y_{n,\gamma}^{calc}}{n_s} = \frac{\int_{T_n^{min}}^{T_n^{max}} \sigma_{n,\gamma}(T_n) \frac{dY}{dT_n}(T_n) dT_n}{\int_{T_n^{min}}^{T_n^{max}} \frac{dY}{dT_n}(T_n) dT_n} \qquad (20)$$

where $\sigma_{n,\gamma}(T_n)$ is the ^{197}Au$(n, \gamma)^{198}$Au reaction cross section from ENDF/B-VIII.0 [30].

To determine $Y_{n,\gamma}^{calc}$, a Monte Carlo simulation of the experiment was performed where the gold foil and the target structure in the neutron direction were included. Emitted neutrons were homogeneously sampled in position from a circular surface of 4 mm diameter, resembling the beam spot defined by the collimator. The code PLINBE also generates a detailed MCNP source file for further transport of neutrons. The source is organized considering first the neutron emission angle, using the calculated angular distribution. From the energy distribution, according to the selected angle, the neutron energy is sampled.

In the simulation, the number of ^{198}Au nuclei formed per source neutron $Y_{n,\gamma}^{calc}$ is calculated. Figure 9 shows the results of this calculation as a function of the proton energy with a FWHM = 1.25 keV.

Working quite close to the reaction threshold has two advantages concerning the gold irradiation. First, due to the reaction kinematics, a forward-directed neutron field is produced with a Gaussian-like energy distribution. The mean energy of this field is 30 keV and varies little with T_p. Around $T_p = 1881.08$ keV, represented by a dot in Fig. 9, the capture rate is constant. As a consequence, the uncertainty in proton energy determination in order to calculate the neutron energy spectrum has no impact in $\langle \sigma_{n,\gamma} \rangle$.

The second advantage is related to the necessary correction when flat samples are used. This is because neutrons emitted

TABLE II. Main parameters and results from gold activation.

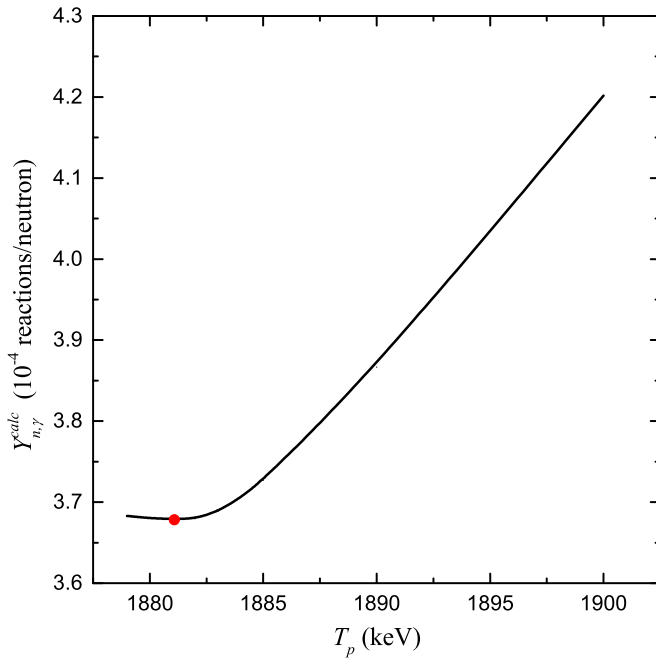| Sample	Mass (g)	Diameter (mm)	n_s (atoms/b)	Neutrons	^{198}Au	$Y_{n,\gamma}$ (reactions/neutron)
1	0.2161 ± 0.0001	11.72 ± 0.05	$(6.11 \pm 0.03) \times 10^{-4}$	4.6×10^9	1.69×10^6	$(3.64 \pm 0.04) \times 10^{-4}$
2	0.2150 ± 0.0001	11.71 ± 0.05		3.3×10^9	1.19×10^6	

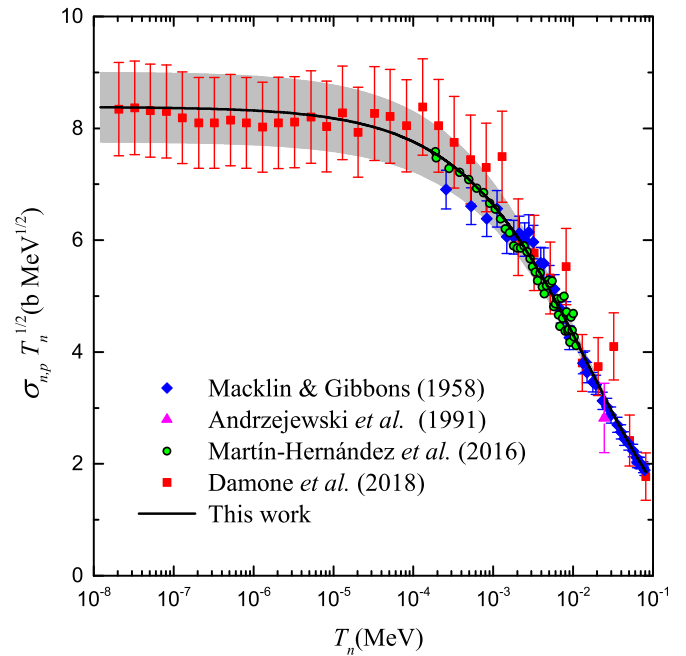FIG. 9. Calculated capture rate in the gold foil as a function of proton energy with FWHM = 1.25 keV. The dot indicates the energy value chosen in this work.

FIG. 10. The ^{7}Be$(n, p)^7$Li reduced reaction cross section determined in this work compared with previous measurements.

at larger angles travel a longer distance within the sample than neutrons emitted at smaller angles. Considering the small opening angle of the neutron field working near T_{th}, the correction due to the use of flat samples is small.

The correction factor is equal to $F_x = 0.97$; that is to say, the experiment departs by 3% from the ideal one.

Table III reproduces the measured $\langle \sigma_{n,\gamma} \rangle$ and includes the calculated one using the evaluated cross section from Carlson *et al.* [9] and the measured one from Massimi *et al.* [31].

F. ^{7}Be$(n, p)^7$Li reaction cross section

The cross section for the time-reversed ^{7}Be$(n, p)^7$Li reaction is calculated using the detailed balance principle. In this case it is reduced to $\sigma_{n,p} = \left(\frac{k_p}{k_n}\right)^2 \sigma_{p,n}$, where k_p and k_n are the wave numbers in the proton and neutron channels and $\sigma_{p,n}$ is the calculated cross section of this work based on thick target yield measurement.

Figure 10 shows this cross section in its reduced form $\sigma_{n,p}\sqrt{T_n}$ as a function of the neutron energy T_n. Four datasets also are included: (i) a direct measurement at $T_n = $

TABLE III. Measured $\langle \sigma_{n,\gamma} \rangle$ and calculated from other references for the neutron spectrum of Fig. 3(a).

Source for ^{197}Au $\sigma_{n,\gamma}(T_n)$	$\langle \sigma_{n,\gamma} \rangle$ (b)
Massimi *et al.* (2014)	0.573 ± 0.007[a]
Carlson *et al.* (2018)	0.585 ± 0.011[b]
This work	0.578 ± 0.007

[a]Prompt γ. Differential measurement by TOF.
[b]Evaluation. GMAP code. Fit of all available data.

24.5 keV [32], (ii) the calculated one applying the detailed balance principle to the Macklin and Gibbons data based on total neutron counting [27], (iii) the calculated one applying the detailed balance principle to Martín-Hernández *et al.* data relative to the ^{10}B$(n, \alpha\gamma)^7$Li reaction [7], and (iv) a recent direct measurement [33].

The uncertainty in the cross section for Damone *et al.* data includes not only the statistical one, as graphically reported in that work, but also a 10% systematic uncertainty mainly due to the sample inhomogeneity. The gray area comprises the uncertainty of our determination.

The cross section datasets plotted in Fig. 10 are taken with different methods and, as is visible, they are in a remarkably good agreement within the quoted uncertainties. It is of particular interest that the last energy decade has a larger impact on the lithium yield according to the big bang nucleosynthesis theory. Therefore, considering the small uncertainty of the cross section in this energy range and the concurrence of the remaining data, it is plausible to exclude the possibility of an incorrect ^{7}Be$(n, p)^7$Li cross section as a cause for the cosmological lithium problem.

V. CONCLUSION

Measurements have been performed at the 7-MV CN Van de Graaff accelerator in the Laboratori Nazionali di Legnaro to determine the thick target yield of the ^{7}Li$(p, n)^7$Be reaction. Thirty-three thick lithium targets were irradiated with incident proton energy from threshold to 1960 keV. Reaction rates from 10^{-4} reactions/pC to nearly 10^2 reactions/pC were measured. Based on the reaction theory a computer code was developed in order to calculate the reaction yield, neutron spectrum, angular distribution, and to generate a MCNP input

file for further transport of neutrons. Using this code, a fitting procedure allowed us to obtain experimental parameters such as proton beam energy and energy spread.

Our thick target yield calculation, describing the reaction cross section with a single level Breit-Wigner shape, accurately reproduces the measured values. The ratio between neutron and proton widths was found to be equal to $\Gamma_n/\Gamma_p = (5.4 \pm 0.4)\sqrt{1 - T_{th}/T_p}$. The accuracy of this ratio has been improved 2.3 times with respect to earlier determinations.

The experiment designed for measuring the ^{197}Au(n, γ) ^{198}Au spectrum-averaged cross section considerably reduces the amount of corrections and uncertainties typical in this kind of measurements. For a Gaussian-like neutron beam with 30 keV of mean energy and 11 keV FWHM, the ^{197}Au$(n, \gamma)^{198}$Au cross section is 0.578 ± 0.007 b. This value is in very good agreement with the calculated value using the reaction cross section from the ENDF/B-VIII.0 library. This result is a step forward in establishing the ^{197}Au$(n, \gamma)^{198}$Au reaction cross section as a standard at around 30 keV of neutron energy.

If the detailed balance principle is not called into question, we state that the ^{7}Be$(n, p)^7$Li reaction cross section is not large enough to guarantee a higher ^{7}Be burning rate during the big bang nucleosynthesis phase of the early Universe.

ACKNOWLEDGMENTS

[1] H. Beer and F. Kappeler, Phys. Rev. C **21**, 534 (1980).

[2] R. Reifarth, C. Lederer and F. Kappeler, J. Phys. G: Nucl. Part. Phys. **41**, 053101 (2014).

[3] C.-K. C. Wang, T. E. Blue, and R. Gahbauer, Nucl. Technol. **84**, 94 (1989).

[4] E. Musacchio González and G. Martín-Hernández, Nucl. Instrum. Methods Phys. Res. A **865**, 148 (2017).

[5] W. Matysiak, W. V. Prestwicha, and S. H. Byun, Nucl. Instrum. Methods Phys. Res. A **643**, 47 (2011).

[6] M. Friedman, D. Cohen, M. Paul, D. Berkovits, Y. Eisen, G. Feinberg, G. Giorginis, S. Halfon, A. Krasa, A. J. M. Plompen, and A. Shor, Nucl. Instrum. Methods Phys. Res. A **698**, 117 (2013).

[7] G. Martín-Hernández, P. Mastinu, M. Maggiore, L. Pranovi, G. Prete, J. Praena, R. Capote-Noy, F. Gramegna, A. Lombardi, L. Maran, C. Scian, and E. Munaron, Phys. Rev. C **94**, 034620 (2016).

[8] R. H. Cyburt, B. D. Fields, K. A. Olive, and T.-H. Yeh, Rev. Mod. Phys. **88**, 015004 (2016).

[9] A. D. Carlson *et al.*, Nucl. Data Sheets **148**, 143 (2018).

[10] J. B. Marion and J. L. Fowler, *Fast Neutron Physics* (Interscience, New York, 1960).

[11] A. Ritchie, J. Phys. D: Appl. Phys. **9**, 15 (1976).

[12] C. L. Lee and X.-L. Zhou, Nucl. Instrum. Methods Phys. Res. B **152**, 1 (1999).

[13] H. W. Newson, R. M. Williamson, K. W. Jones, J. H. Gibbons, and H. Marshak, Phys. Rev. **108**, 1294 (1957).

[14] J. F. Ziegler, J. P. Biersack, and M. D. Ziegler, *SRIM - the stopping and range of ions in matter*, SRIM Co., Maryland, 2008.

[15] F. Heisse, F. Kohler-Langes, S. Rau, J. Hou, S. Junck, A. Kracke, A. Mooser, W. Quint, S. Ulmer, G. Werth, K. Blaum, and S. Sturm, Phys. Rev. Lett. **119**, 033001 (2017).

[16] M. Wang, G. Audi, F. G. Kondev, W. J. Huang, S. Naimi, and X. Xu, Chin. Phys. C **41**, 030003 (2017).

[17] W. J. Huang, G. Audi, M. Wang, F. G. Kondev, S. Naimi, and X. Xu, Chin. Phys. C **41**, 030002 (2017).

[18] J. Meija, T. B. Coplen, M. Berglund, W. A. Brand, P. Biévre, M. Gröning, N. E. Holden, J. Irrgeher, R. D. Loss, T. Walczyk, and T. Prohaska, Pure Appl. Chem. **88**, 265 (2016).

[19] J. K. Tuli, Nuclear Wallet Cards, 2011, https://www.nndc.bnl.gov/wallet

[20] The NIST Reference on Constants, Units, and Uncertainty, http://physics.nist.gov/constants

[21] N. Otuka and S. Takacs, Radiochim. Acta **103**, 1 (2015).

[22] D. R. Tilley, C. M. Cheves, J. L. Godwin, G. M. Hale, H. M. Hofmann, J. H. Kelley, C. G. Sheu, and H. R. Weller, Nucl. Phys. A **708**, 3 (2002).

[23] X-5 Monte Carlo Team, MCNP - A General Monte Carlo N-Particle Transport Code, Version 5, LA-UR-03-1987, 2005.

[24] X. Huang and M. Kang, Nucl. Data Sheets **133**, 221 (2016).

[25] H. Paul and A. Schinner, Nucl. Instrum. Methods Phys. Res. B **227**, 461 (2005).

[26] J. F. Ziegler, M. D. Ziegler, and J. P. Biersack, Nucl. Instrum. Methods Phys. Res. B **268**, 1818 (2010).

[27] R. L. Macklin and J. H. Gibbons, Phys. Rev. **109**, 105 (1958).

[28] R. Taschek and A. Hemmendinger, Phys. Rev. **74**, 373 (1948).

[29] K. K. Sekharan, H. Laumer, B. D. Kern, and F. Gabbard, Nucl. Instrum. Methods **133**, 253 (1976).

[30] D. A. Brown *et al.*, Nucl. Data Sheets **148**, 1 (2018).

[31] C. Massimi, B. Becker, E. Dupont, S. Kopecky, C. Lampoudis, R. Massarczyk, M. Moxon, V. Pronyaev, P. Schillebeeckx, I. Sirakov, and R. Wynants, Eur. Phys. J. A **50**, 124 (2014).

[32] J. Andrzejewski, Yu. M. Gledenov, Yu. P. Popov, V. I. Salatski, and V. A. Pshenichnyj, Z. Phys. A **340**, 105 (1991).

[33] L. Damone *et al.*, Phys. Rev. Lett. **121**, 042701 (2018).